ACS APPLIED MATERIALS & INTERFACES
Research Article
www.acsami.org

Thermoelectric Properties of Ga/Ag Codoped Type-III $Ba_{24}Ge_{100}$ Clathrates with in Situ Nanostructures

Jiefei Fu,[†] Xianli Su,[*,†] Yun Zheng,[†] Hongyao Xie,[†] Yonggao Yan,[†] Xinfeng Tang,[*,†] and Ctirad Uher[‡]

[†]State Key Laboratory of Advanced Technology for Materials Synthesis and Processing, Wuhan University of Technology, Wuhan 430070, China

[‡]Department of Physics, University of Michigan, Ann Arbor, Michigan 48109, United States

ABSTRACT: Because of the low thermal conductivity and high electrical conductivity, type-III $Ba_{24}Ge_{100}$ clathrates are potentially of interest as power generation thermoelectric materials for midto-high temperature operations. Unfortunately, their too high intrinsic carrier concentration results in a quite low Seebeck coefficient. To reduce the carrier concentration, we prepared a series of Ga/Ag codoped type-III $Ba_{24}Ge_{100}$ clathrate specimens by vacuum melting and subsequently compacted by spark plasma sintering (SPS). Doping Ga−Ag on the sites of Ge reduces the concentration of electrons and, at higher concentrations, also leads to the in situ formation of $BaGe_2$ nanoprecipitates detected by the microstructural analysis. As a result of doping, the Seebeck coefficient increases, the thermal conductivity decreases, and the dimensionless figure of merit ZT reaches a value of 0.34 at 873 K, more than three times the value obtained with undoped $Ba_{24}Ge_{100}$.

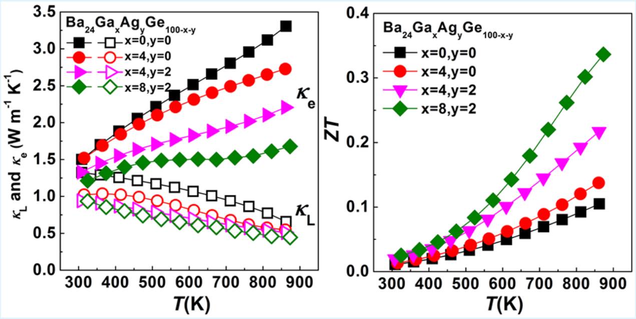

KEYWORDS: *codoping, carrier concentration, nanoprecipitates, thermoelectric properties, type-III clathrates*

1. INTRODUCTION

With the increasing concerns regarding a rapid depletion of fossil fuels, there is a strong need to find alternative energy sources. Thermoelectric (TE) energy conversion is a highly reliable solid state technology able to convert waste industrial heat into electricity[1] and has attracted a worldwide attention in recent years. The performance of a thermoelectric material is evaluated by the magnitude of the dimensionless figure of merit $ZT = \alpha^2\sigma T/\kappa$, where α, σ, κ, and T are the Seebeck coefficient, the electrical conductivity, the thermal conductivity and the absolute temperature, respectively.[2] Because of a strong interdependence of the three transport parameters (α, σ, and κ), it is a challenge to optimize ZT. The electronic properties, often specified by the power factor $PF = \alpha^2\sigma$, are closely related to the carrier concentration and thus optimizing the carrier concentration (n) is crucial for achieving high performance. At the same time, a good thermoelectric material must have a low thermal conductivity.

Clathrate compounds with their polyhedral cages and encapsulated guest atoms are considered to behave as phonon glass-electron crystal (PGEC) materials.[3−7] The polyhedral cages generally consist of Group IV and Group III elements, while alkali metal atoms or alkaline earth metal atoms reside inside the cages as guest atoms. There are several types of clathrate compounds designated as type-I,[8−11] type-II,[12−14] type-III,[15−25] and type-VIII[26−28] clathrates. Type III $Ba_{24}Ge_{100}$ clathrate compounds are composed of three kinds of cage structures including pentagonal dodecahedrons, open dodecahedrons, and distorted cubes,[20−23] as shown in Figure 1. As a consequence of their complex structure, the thermal conductivity of clathrates is intrinsically very low. The structure contains both 3-fold bonded (3b) and 4-fold bonded (4b) Ge atoms. According to the Zintl concept, $Ba_{24}Ge_{100}$ can be written as $[Ba^{2+}]_{24}[(3b)Ge^-]_{32}[(4b)Ge^0]_{68}[16e^-]$, and thus 16 conduction electrons are present in $Ba_{24}Ge_{100}$.[16] As a result, type-III $Ba_{24}Ge_{100}$ clathrate compounds behave as n-type heavily doped semiconductor with the carrier concentration of approximately 5×10^{21} cm^{-3} at room temperature. Compared with other clathrates, the type-III $Ba_{24}Ge_{100}$ clathrates possess low thermal conductivity and high electrical conductivity (about 2×10^5 Sm^{-1}) at ambient temperature.[16] The intrinsically low thermal conductivity and high electrical conductivity render these materials as a potentially useful high temperature thermoelectric. However, because of the high carrier concentration, the Seebeck coefficient of $Ba_{24}Ge_{100}$ is relatively low, resulting in a low power factor. Consequently, it is essential to reduce the carrier concentration so that the Seebeck coefficient and with it the thermoelectric performance of type-III $Ba_{24}Ge_{100}$ clathrates could be improved.

Recently, several attempts have been made to enhance the Seebeck coefficient of $Ba_{24}Ge_{100}$ clathrates by reducing the concentration of electrons via acceptor doping. By doping with

Received: June 4, 2015
Accepted: August 17, 2015
Published: August 17, 2015

DOI: 10.1021/acsami.5b04910
ACS Appl. Mater. Interfaces 2015, 7, 19172−19178

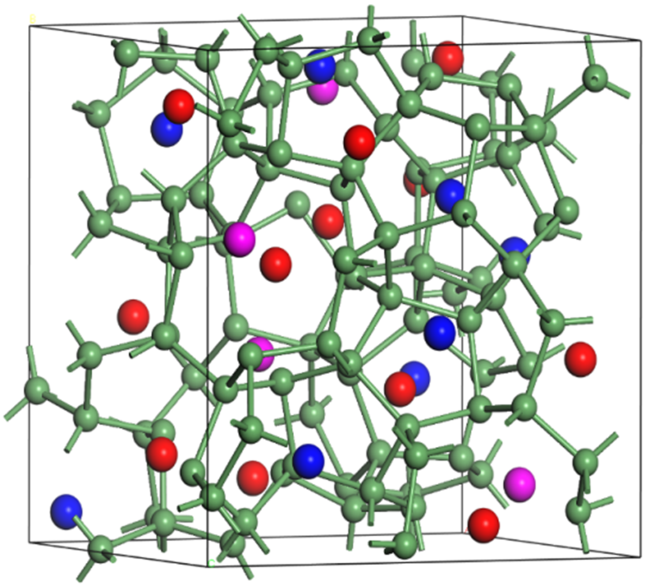

Figure 1. Structure of $Ba_{24}Ge_{100}$ clathrates. Green atoms are Ge atoms; blue, red, and pink atoms refer to three crystallographically different Ba atoms.

the Group IIIA elements (Al, Ga, In) on Ge sites[17−19] the *ZT* was, indeed, improved however the carrier concentration still remained very high due to a small difference in the valence of Ga and Ge where the Ga atom on the site of Ge can give rise to no more than one hole. In principle, a more effective suppression of electrons in $Ba_{24}Ge_{100}$ clathrates should be achieved by doping Group IB elements (Cu, Ag) at Ge sites. In this case, an atom such as Ag should introduce more than one hole, resulting in a stronger compensation of electrons. However, because of the larger incompatibility between IB elements and Ge, one may not be able to substitute as many IB atoms as in the case of IIIA elements, in other words, the solubility limit for IB elements in $Ba_{24}Ge_{100}$ is likely to be lower.

In this study, to simultaneously increase the Seebeck coefficient and lower the lattice thermal conductivity, we codoped $Ba_{24}Ge_{100}$ with Ga and Ag. The samples were synthesized by vacuum melting combined with a subsequent application of spark plasma sintering (SPS). The impact of Ga and Ag contents on the microstructure and thermoelectric properties of type-III clathrate compounds was carefully evaluated.

2. EXPERIMENTAL SECTION

High-purity Ba chunks (2N), Ag wires (4N), Ga shots (5N), and Ge bulks (4N) were weighed in the glovebox according to the stoichiometry of $Ba_{24}Ga_xAg_yGe_{100-x-y}$ (x = 0, 4, 8, 10, y = 1, 2). Carbon crucibles containing raw materials were placed in silica tubes which were then vacuum-sealed (~1 × 10^{-3} Torr) and loaded into a vertical furnace. The samples were heated to 1273 K in 5 h, maintained at this temperature for 10 h and then allowed to furnace cool. The obtained ingots were hand-ground into fine powders and densified by SPS in a 15 mm diameter graphite die under vacuum. The sintering was done at 923 K under 35 MPa for 10 min.

Phase compositions were determined by powder X-ray diffraction (XRD, CuK_α PANalytical Empyrean, Netherlands). Microstructures of bulk specimens were investigated by field-emission scanning electron microscopy (FESEM, Hitachi SU-8020, Japan) and transmission electron microscopy (TEM, JEM-2100F, JEOL, Japan) equipped with an energy-dispersive X-ray spectrometer (EDS). The electrical conductivity (σ) and the Seebeck coefficient (α) were measured at 300−973 K by a standard four-probe method (ZEM-3, ULVAC-RIKO, Japan). The Hall coefficient (R_H) was measured using a Physical Properties Measurement System (PPMS-9, Quantum Design, USA). The carrier concentration (n) and the Hall mobility (μ_H) were calculated from $n = 1/e|R_H|$ and $\mu_H = \sigma|R_H|$, respectively. Thermal conductivities were calculated from measurements of the thermal diffusivity D (the laser flash method using LFA 457, Netzsch), the specific heat C_p (differential scanning calorimeter DSC Q20, TA Instruments), and the sample density ρ(the Archimedes' method) using an equation $\kappa = DC_p\rho$. The relative densities of all samples were over 95%.

3. RESULTS AND DISCUSSION

Powder X-ray diffraction (XRD) patterns for the $Ba_{24}Ga_xGe_{100-x}$ (x = 0, 4, 8, 10) and $Ba_{24}Ga_xAg_yGe_{100-x-y}$ (x = 4, 8, y = 1, 2) samples after SPS are shown in Figure 2a, b, respectively. All patterns can be indexed to the $Ba_{24}Ge_{100}$ phase (JCPDS 98−041−4380). As shown in Figure 2a, a single phase type-III clathrate is obtained for the sample with the Ga content less than 8%. When the Ga content exceeds 8%, the type-I clathrate phase is detected in the XRD pattern and its fraction increases with the increasing content of Ga. The solubility limit of Ga in $Ba_{24}Ga_xGe_{100-x}$ is thus about 8%, a value lower than reported by Kim.[17] As Figure 2b indicates, $Ba_{24}Ga_4Ag_1Ge_{95}$ form as single phase. However, with the increasing content of Ga, the type-I clathrate phase is observed in the specimen with

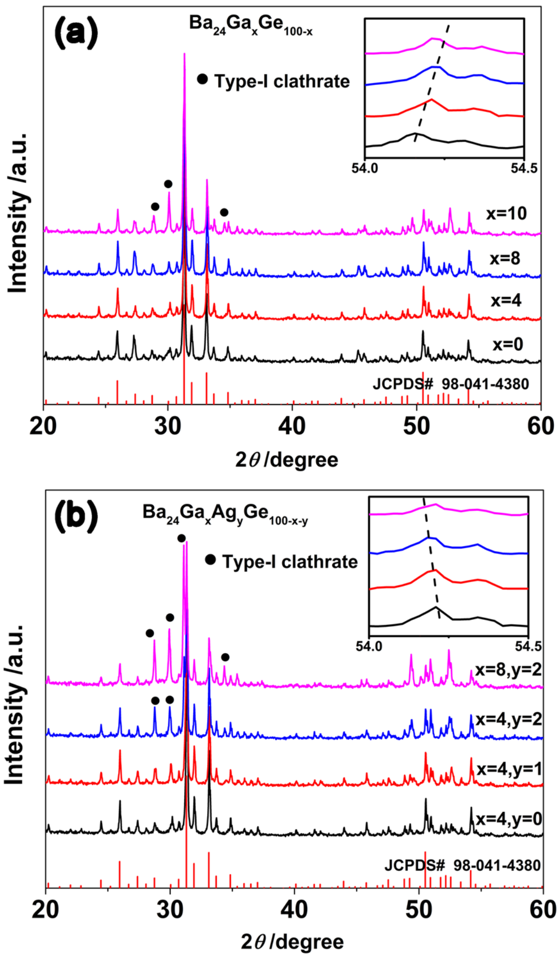

Figure 2. Powder X-ray diffraction patterns of (a) $Ba_{24}Ga_xGe_{100-x}$ and (b) $Ba_{24}Ga_xAg_yGe_{100-x-y}$ samples after SPS. Insets in a and b show the expand view of XRD pattern from 54.0 to 54.5.

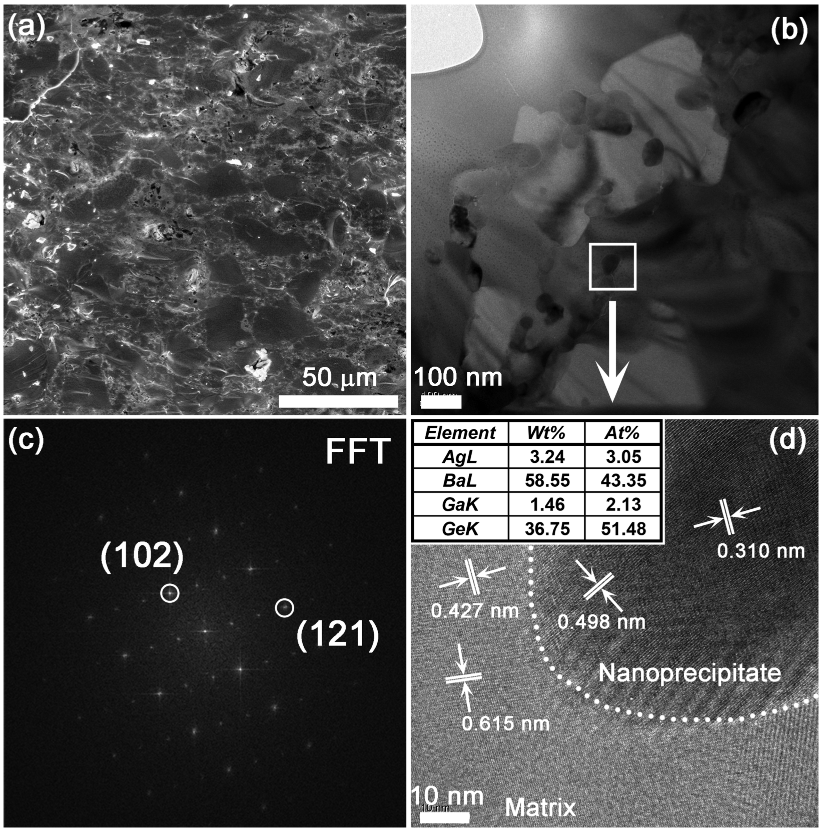

Element	Wt%	At%
AgL	3.24	3.05
BaL	58.55	43.35
GaK	1.46	2.13
GeK	36.75	51.48

Figure 3. $Ba_{24}Ga_8Ag_2Ge_{90}$ (a) FESEM image, (b) HRTEM image, (c) FFT image of the area surrounded by the dashed line of d, (d) enlarged view of b, inset in d shows the EDS results for the nanoparticle.

Table 1. Hall Coefficient R_H, Carrier Concentration n, Hall Mobility μ_H, Seebeck Coefficient α, and Electrical Conductivity for $Ba_{24}Ga_xAg_yGe_{100-x-y}$ Specimens at 300 K

x y	compd	R_H ($\times 10^{-3} cm^3/C$)	n ($\times 10^{21} cm^{-3}$)	μ_H ($cm^2 V^{-1} s^{-1}$)	α ($\mu V/K$)	σ ($\times 10^4 Sm^{-1}$)
$x = 0$	$Ba_{24}Ge_{100}$	−1.14	5.50	2.32	−23.13	20.34
$x = 4$	$Ba_{24}Ga_4Ge_{96}$	−1.73	3.63	3.49	−23.89	20.23
$x = 8$	$Ba_{24}Ga_8Ge_{92}$	−2.15	2.83	3.55	−29.82	16.49
$x = 4$ $y = 2$	$Ba_{24}Ga_4Ag_2Ge_{94}$	−2.79	2.23	5.10	−28.01	18.28
$x = 8$ $y = 2$	$Ba_{24}Ga_8Ag_2Ge_{90}$	−4.91	1.27	7.84	−32.04	15.97

nominal composition of $Ba_{24}Ga_8Ag_2Ge_{90}$. The inset of Figure 2a, b show that the expanded view of XRD pattern for higher angle (54.0−54.5). With the increase in Ga content, XRD peaks shift toward higher angle, indicating the lattice parameter decrease with the increase of Ga content, whereas for the Ag-doped type-III chlatrate, XRD peaks shift toward lower angle, indicating the lattice parameter increase with the increase of Ag content. As the content of Ga and Ag increases, the type-III clathrate structure becomes unstable because of an electrostatic imbalance and strain in the crystal lattice, which gives rise to the presence of the type-I clathrate in the XRD pattern.

To observe and assess the microstructure of our $Ba_{24}Ga_8Ag_2Ge_{90}$ sample, we employed field-emission scanning electron microscopy (FESEM) and high-resolution transmission electron microscopy (HRTEM). The respective images are shown in Figure 3. Figure 3a indicates that the obtained bulk material is fully compacted. Figure 3b depicts nanoparticles with the size of about 50 nm embedded in the matrix. Fast Fourier transform (FFT) and EDS results, Figure 3c, d shows that the nanoparticles are $BaGe_2$. The interplanar spacings in the nanoparticles were calculated to be 0.498 and 0.310 nm, corresponding to (101) and (121) planes of $BaGe_2$, respectively. The coexistence of $BaGe_2$ nanoinclusions and type-I clathrate phases is expected to exert a significant influence on the thermal and electronic transport properties.

On the basis of the Zintl concept, $Ba_{24}Ge_{100}$ can be written as $[Ba^{2+}]_{24}[(3b)Ge^{-}]_{32}[(4b)Ge^{0}]_{68}[16e^{-}]$, thus 16 conduction electrons are expected in $Ba_{24}Ge_{100}$.[16] As already noted, we used Ga/Ag codoping on sites of Ge in an attempt to decrease the concentration of electrons. Room temperature transport properties are summarized in Table 1, including the Hall coefficient R_H, the carrier concentration n, the Hall mobility μ_H, the Seebeck coefficient α, and the electrical conductivity σ of $Ba_{24}Ga_xAg_yGe_{100-x-y}$ samples. The Hall coefficient R_H is negative indicating n-type conduction. The carrier concentration of pristine $Ba_{24}Ge_{100}$ is 5.5×10^{21} cm^{-3} at 300 K, which is consistent with the literature data.[16] The carrier concentration of the Ga/Ag codoped $Ba_{24}Ga_4Ag_2Ge_{94}$ sample (2.23×10^{21} cm^{-3}) is much lower than the carrier concentration of just Ga-doped $Ba_{24}Ga_8Ge_{92}$ sample (3.55×10^{21} cm^{-3}). Although the substitution percentage on Ge site in $Ba_{24}Ga_8Ge_{92}$ is much higher than in that in $Ba_{24}Ga_4Ag_2Ge_{94}$, the concentration of

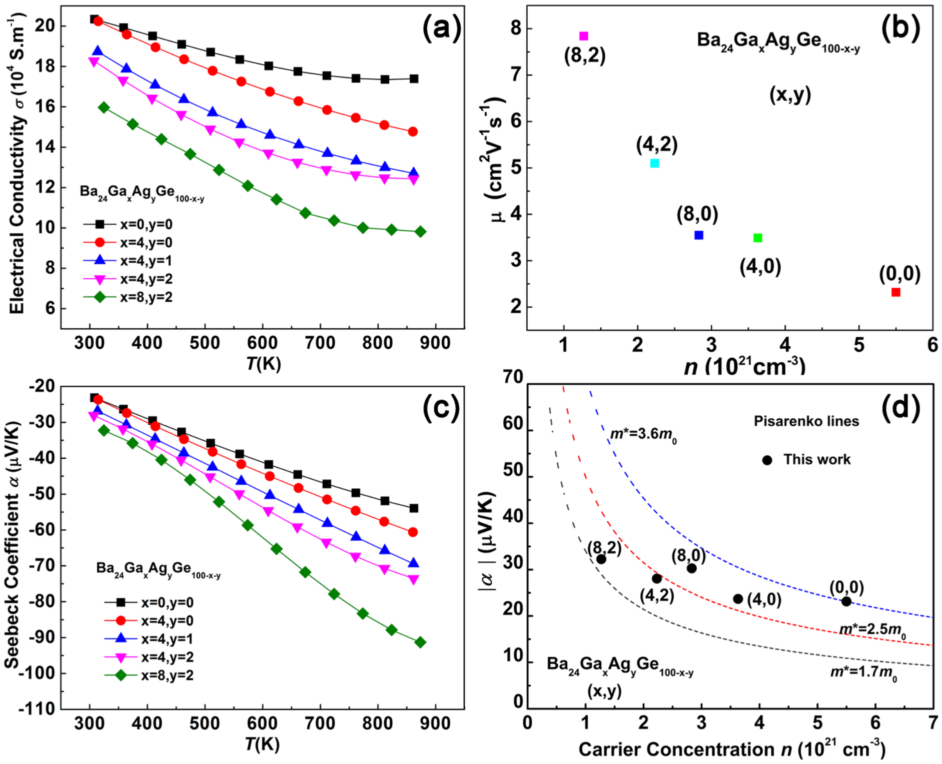

Figure 4. Temperature dependence of (a) electrical conductivity, (b) Hall mobility μ_H and (c) Seebeck coefficient of $Ba_{24}Ga_xAg_yGe_{100-x-y}$ specimens as a function of the carrier concentration. (d) Pisarenko plots showing the measured Seebeck coefficients at 300 K of $Ba_{24}Ga_xAg_yGe_{100-x-y}$ specimens as a function of the carrier concentration.

electrons in the former is significantly higher than in the latter specimen. This indicates that Ga is not as effective in suppressing the density of electrons as is Ag. The beneficial presence of Ag as a dopant is also apparent in the $Ba_{24}Ga_8Ag_2Ge_{90}$ sample where the carrier density is reduced down to 1.27×10^{21} cm^{-3}, a reduction of more than a factor of 4 in comparison to the carrier density in $Ba_{24}Ge_{100}$ and less than half of the carrier density in $Ba_{24}Ga_8Ge_{92}$.

Temperature dependence of the electrical conductivity and the Seebeck coefficient for all $Ba_{24}Ga_xAg_yGe_{100-x-y}$ specimens is shown in Figure 4. As the content of Ga and Ag increases, the electrical conductivity decreases, reflecting the reduced carrier density. Surprisingly, the Hall mobility seems to increase with the increasing content of dopants, suggesting that impurity scattering may not be damaging to electron transport to the extent the carrier−carrier interaction is. The Seebeck coefficient and hall measurement indicate n-type conduction. The absolute value of the Seebeck coefficient increases as Ga and Ag contents increase, i.e., inversely related to the behavior of the carrier concentration and electrical conductivity. Assuming the carrier mean free path is independent of energy, the Seebeck coefficient of a degenerate semiconductor can be expressed by the following equation

$$\alpha = \frac{8\pi^2 k_B^2 T}{3eh^2} m^* \left(\frac{\pi}{3n}\right)^{2/3} \qquad (1)$$

where n is the carrier concentration, T is the temperature, and m^* is the effective mass, respectively. Although a single parabolic band model might be an oversimplification, it nevertheless provides an insight into the doping effect of Ga and Ag on the transport properties. Figure 4d shows the room temperature Seebeck coefficient as a function of the carrier concentration, i.e., the Pisarenko plots. The effective mass of our samples obtained from the fits ranges from $1.7m_0$ to $3.6m_0$, where m_0 is the free electron mass. The effective mass increases with the increasing carrier concentration, likely the result of nonparabolicity of the conduction band.

The temperature dependence of the power factor for all $Ba_{24}Ga_xAg_yGe_{100-x-y}$ specimens is shown in Figure 5. Because of the enhanced Seebeck coefficient, the calculated power factor of $Ba_{24}Ga_8Ag_2Ge_{90}$ is 0.82×10^{-3} W m^{-1} K^{-2} at 873 K, which is a factor of about two higher in comparison to the power factor of undoped $Ba_{24}Ge_{100}$ (0.47×10^{-3} W m^{-1} K^{-2} at 873 K).

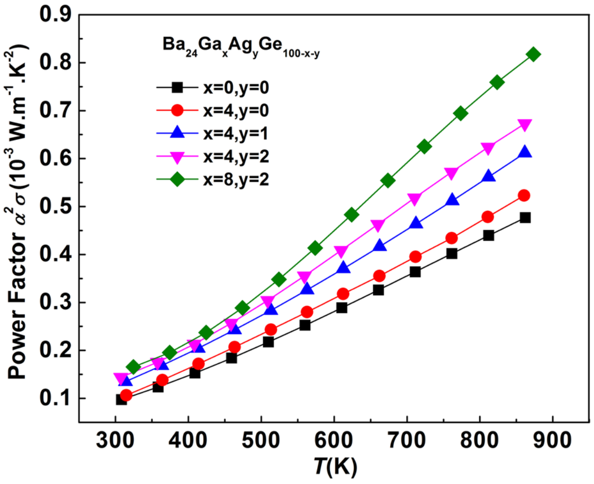

Figure 5. Temperature dependent power factor for $Ba_{24}Ga_xAg_yGe_{100-x-y}$ specimens.

Temperature dependence of the thermal conductivity is plotted in Figure 6. As a comparison, Figure 6a also displays the thermal conductivity of type-I Ba_8Ge_{43} clathrate.[11] Thermal conductivities of both Ba_8Ge_{43} (type-I clathrate) and $Ba_{24}Ge_{100}$ (type-III clathrate) are quite high. The thermal conductivity of $Ba_{24}Ge_{100}$ increases linearly with temperature from a value of 2.8 W m^{-1} K^{-1} at room temperature to 4.0 W m^{-1} K^{-1} at 873 K. Doping the structure results in a decreased thermal conductivity due to enhanced alloy scattering together with the lower electronic thermal conductivity. In general, the total thermal conductivity $\kappa = \kappa_L + \kappa_e$, consists of the lattice component κ_L and the electronic thermal conductivity κ_e which can be estimated by using the Wiedemann−Franz law, $\kappa_e = L_0 \sigma T$. The Lorenz number L_0 can be calculated under the assumption of a single parabolic band model within the relaxation time approximation and assuming the dominance of acoustic phonon scattering[29−31] from the following two equations

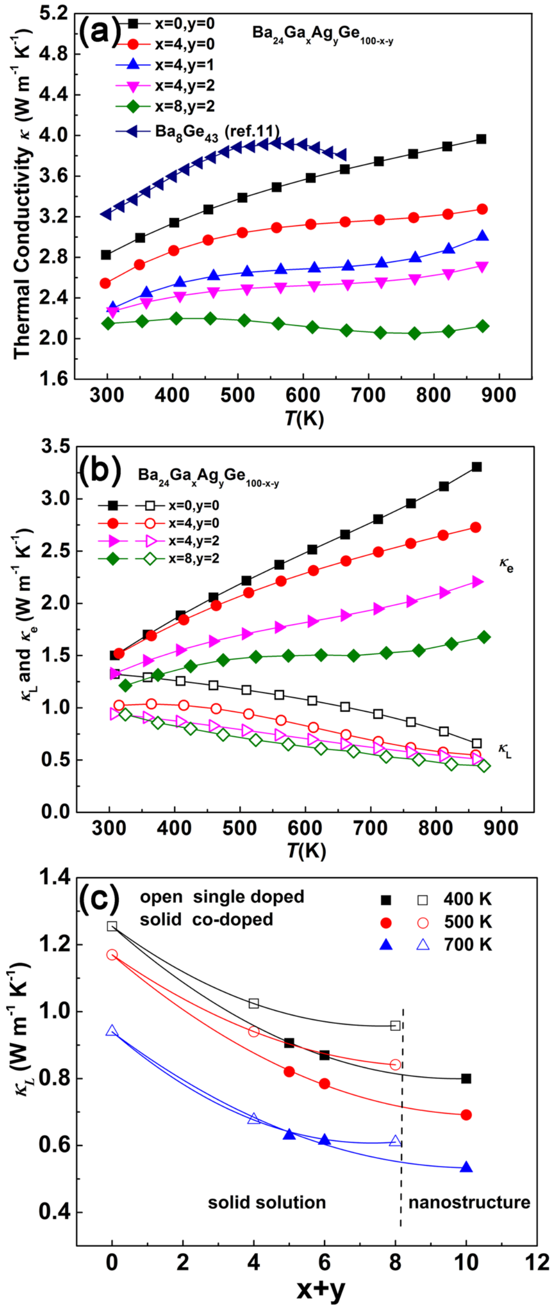

Figure 6. Temperature dependence of (a) the thermal conductivity and (b) the lattice and the electronic parts of the thermal conductivity of $Ba_{24}Ga_xAg_yGe_{100-x-y}$ specimens. (c) Lattice thermal conductivity at 400, 500, and 700 K as a function of the doping content of $Ba_{24}Ga_xAg_yGe_{100-x-y}$ specimens. Open symbols refer to samples doped with only Ga, solid symbols represent Ga/Ag double-doped samples. The vertical dashed line indicates a regime of doping above which nanoinclusions of $BaGe_2$ are detected in the structure.

$$L_0 = \left(\frac{k_B}{e}\right)^2 \frac{3F_0(\eta)F_2(\eta) - 4F_1(\eta)^2}{F_0(\eta)^2} \tag{2}$$

$$\alpha = -\frac{k_B}{e}\left[\frac{2F_1(\eta)}{F_0(\eta)} - \eta\right] \tag{3}$$

Here, η is the reduced Fermi level, $F_n(\eta)$ refers to the Fermi integral of order n, k_B is the Boltzmann constant, and e is the electron charge, respectively. With the reduced Fermi level the calculated Lorenz number L_0 falls in the range from 2.39 to 1.95. Subtracting the electronic part, one obtains the lattice thermal conductivity. The lattice thermal conductivity of $Ba_{24}Ga_xAg_yGe_{100-x-y}$ specimens decreases with the increasing content of Ga/Ag and decreases with the increasing temperature. The dependence on the type and the content of dopants is presented in Figure 6c where open symbols and solid symbols represent, respectively, the lattice thermal conductivity of Ga-doped (single dopant) $Ba_{24}Ga_xGe_{100-x}$ and Ga/Ag codoped $Ba_{24}Ga_xAg_yGe_{100-x-y}$ samples at different temperatures. It is evident that, for comparable doping contents, the lattice thermal conductivity of the codoped sample is much lower than the thermal conductivity of the sample doped with just Ga. Maybe Ga/Ag codoping could affect a broader range of phonon frequencies in comparison to doping with only Ga, a situation reminiscent of multiple-filled skutterudites.[32,33] When the doping content exceeds $x = 8$, apart from alloy scattering, the lattice thermal conductivity is further suppressed because of enhanced interface scattering and grain boundary scattering of phonons on nanoinclusions of $BaGe_2$. The lowest lattice thermal conductivity of 0.45 W m^{-1} K^{-1} at 873 K is obtained for the $Ba_{24}Ga_8Ag_2Ge_{90}$ specimen.

Figure 7 shows the temperature dependence of the dimensionless figure of merit ZT. The peak ZT value of pure $Ba_{24}Ge_{100}$ is about 0.1 at 873 K, in agreement with the reported value.[17] Ga/Ag codoping not only reduces the carrier concentration but it also enhances alloy scattering and thus lowers the thermal conductivity. Moreover, as already noted, at high doping contents (above $x = 8$), the nanoprecipitates of $BaGe_2$ lower the thermal conductivity further because of enhanced boundary scattering of heat-conducting phonons. Improved power factors combined with the reduced thermal conductivity lead to a significantly improved figure of merit which reaches 0.34 at 873 K for the Ga/Ag codoped $Ba_{24}Ga_8Ag_2Ge_{90}$ specimen, an improvement by a factor of more than 3 compared to undoped $Ba_{24}Ge_{100}$.

4. CONCLUSIONS

Ga/Ag codoped $Ba_{24}Ge_{100}$ samples were synthesized by a vacuum melting combined with the SPS process. With the increasing Ga/Ag doping content, the room temperature carrier concentration gradually decreased from 5.5 × 10^{21} cm^{-3} ($Ba_{24}Ge_{100}$) down to 1.27 × 10^{21} cm^{-3} ($Ba_{24}Ga_8Ag_2Ge_{90}$).

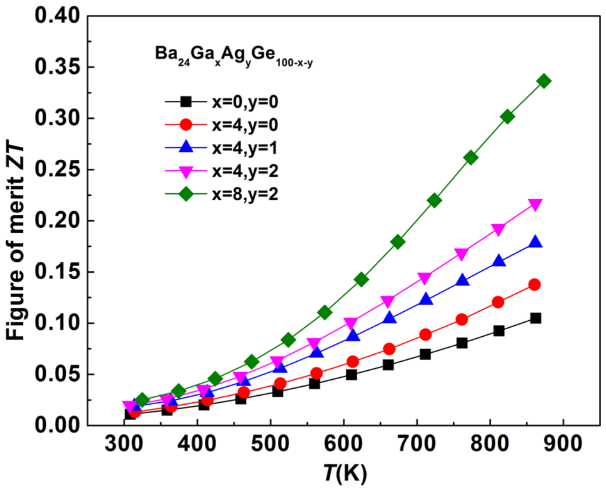

Figure 7. Temperature dependence of *ZT* for $Ba_{24}Ga_xAg_yGe_{100-x-y}$ specimens.

Although this resulted in a somewhat lower electrical conductivity, the carrier mobility actually increased as a consequence of the reduced carrier−carrier scattering. The reduced carrier concentration benefitted the magnitude of the Seebeck coefficient and also resulted in a lower electronic thermal conductivity. Moreover, the presence of dopants in the crystal lattice enhanced alloy scattering of phonons and, at high doping levels, the formation of $BaGe_2$ nanoprecipitates led to increased boundary scattering of heat-conducting phonons, both processes resulting in a degradation of the lattice thermal conductivity. The lowest lattice thermal conductivity of 0.45 W m^{-1} K^{-1} at 873 K was obtained for the $Ba_{24}Ga_8Ag_2Ge_{90}$ specimen. This specimen also recorded the highest dimensionless figure of merit $ZT = 0.34$ at 873 K, the value that was more than a factor of 3 larger than the figure of merit of the undoped $Ba_{24}Ge_{100}$ structure. A further suppression of the concentration of electrons down to a level of $\sim 1 \times 10^{20}$ cm^{-3} is needed to boost the Seebeck coefficient and improve the thermoelectric performance of type-III $Ba_{24}Ge_{100}$-based clathrates. This might possibly be achieved by exploring acceptor doping on the sites of Ba.

■ AUTHOR INFORMATION

Corresponding Authors

*E-mail: suxianli@whut.edu.cn.
*E-mail: tangxf@whut.edu.cn.

Notes

The authors declare no competing financial interest.

■ ACKNOWLEDGMENTS

We wish to acknowledge support from the National Basic Research Program of China (973 program) under Project 2013CB632502, the Natural Science Foundation of China (Grant 51402222, 51172174) and the 111 Project of China (Grant B07040).

■ REFERENCES

(1) Snyder, G. J.; Toberer, E. S. Complex Thermoelectric Materials. *Nat. Mater.* **2008**, *7* (2), 105−114.

(2) Rowe, D. M. *CRCHandbook of Thermoelectrics*; CRC Press: Boca Raton, FL, 1995.

(3) Cahill, D. G.; Watson, S. K.; Pohl, R. O. Lower Limit to the Thermal Conductivity of Disordered Crystals. *Phys. Rev. B: Condens. Matter Mater. Phys.* **1992**, *46* (10), 6131−6140.

(4) Kahn, D.; Lu, J. P. Structural Properties and Vibrational Modes of Si_{34} and Si_{46} Clathrates. *Phys. Rev. B: Condens. Matter Mater. Phys.* **1997**, *56* (21), 13898.

(5) Fang, S.; Grigorian, L.; Eklund, P.; Dresselhaus, G.; Dresselhaus, M.; Kawaji, H.; Yamanaka, S. Raman Sscattering from Vibrational Modes in Si_{46} Clathrates. *Phys. Rev. B: Condens. Matter Mater. Phys.* **1998**, *57* (13), 7686.

(6) Guyot, Y.; Grosvalet, L.; Champagnon, B.; Reny, E.; Cros, C.; Pouchard, M. Grüneisen Parameters for Silicon Clathrates Determined by Raman Scattering. *Phys. Rev. B: Condens. Matter Mater. Phys.* **1999**, *60* (21), 14507.

(7) Tournus, F.; Masenelli, B.; Mélinon, P.; Connétable, D.; Blase, X.; Flank, A. M.; Lagarde, P.; Cros, C.; Pouchard, M. Guest Displacement in Silicon Clathrates. *Phys. Rev. B: Condens. Matter Mater. Phys.* **2004**, *69* (3), No. 035208, DOI: 10.1103/PhysRevB.69.035208.

(8) Shi, X.; Yang, J.; Bai, S.; Yang, J.; Wang, H.; Chi, M.; Salvador, J. R.; Zhang, W.; Chen, L.; Wong-Ng, W. On the Design of High-Efficiency Thermoelectric Clathrates through a Systematic Cross-Substitution of Framework Elements. *Adv. Funct. Mater.* **2010**, *20* (5), 755−763.

(9) Saramat, A.; Svensson, G.; Palmqvist, A. E. C.; Stiewe, C.; Mueller, E.; Platzek, D.; Williams, S. G. K.; Rowe, D. M.; Bryan, J. D.; Stucky, G. D. Large Thermoelectric Figure of Merit at High Temperature in Czochralski-grown Clathrate $Ba_8Ga_{16}Ge_{30}$. *J. Appl. Phys.* **2006**, *99* (2), 023708.

(10) Deng, S.; Tang, X.; Zhang, Q. Synthesis and Thermoelectric Properties of p-type Ba_8Ga $_{16}Zn_xGe_{30-x}$ Type-I Clathrates. *J. Appl. Phys.* **2007**, *102* (4), 043702.

(11) Aydemir, U.; Candolfi, C.; Borrmann, H.; Baitinger, M.; Ormeci, A.; Carrillo-Cabrera, W.; Chubilleau, C.; Lenoir, B.; Dauscher, A.; Oeschler, N. Crystal Structure and Transport Properties of Ba_8Ge_{43}[square]$_3$. *Dalton Trans.* **2010**, *39* (4), 1078−1088.

(12) Nolas, G. S.; Vanderveer, D. G.; Wilkinson, A. P.; Cohn, J. L. Temperature Dependent Structural and Transport Properties of the Type-II Clathrates $A_8Na_{16}E_{136}$ (A = Cs or Rb and E = Ge or Si). *J. Appl. Phys.* **2002**, *91* (11), 8970.

(13) Beekman, M.; Wong-Ng, W.; Kaduk, J. A.; Shapiro, A.; Nolas, G. S. Synthesis and Single-Crystal X-ray Diffraction Studies of New Framework Substituted Type-II Clathrates, $Cs_8Na_{16}Ag_xGe_{136-x}$ ($x <$ 7). *J. Solid State Chem.* **2007**, *180* (3), 1076−1082.

(14) Dong, Y.; Nolas, G. S. Rapid Crystal Growth of Type-II Clathrates $A_8Na_{16}Si_{136}$ (A = K, Rb, Cs) by Spark Plasma Sintering. *CrystEngComm* **2015**, *17* (11), 2242−2244.

(15) Rachi, T.; Yoshino, H.; Kumashiro, R.; Kitajima, M.; Kobayashi, K.; Yokogawa, K.; Murata, K.; Kimura, N.; Aoki, H.; Fukuoka, H.; Yamanaka, S.; Shimotani, H.; Takenobu, T.; Iwasa, Y.; Sasaki, T.; Kobayashi, N.; Miyazaki, Y.; Saito, K.; Guo, F.; Kobayashi, K.; Osaka, K.; Kato, K.; Takata, M.; Tanigaki, K. Superconductivity and Physical Properties of $Ba_{24}Si_{100}$ Determined from Electric Transport, Specific-heat Capacity, and Magnetic Susceptibility Measurements. *Phys. Rev. B: Condens. Matter Mater. Phys.* **2005**, *72* (14), 144504.

(16) Paschen, S.; Tran, V. H.; Baenitz, M.; Carrillo-Cabrera, W.; Grin, Y.; Steglich, F. Clathrate Ba_6Ge_{25}: Thermodynamic, Magnetic, and Transport Properties. *Phys. Rev. B: Condens. Matter Mater. Phys.* **2002**, *65* (13), 134435.

(17) Kim, J.-H.; Okamoto, N. L.; Kishida, K.; Tanaka, K.; Inui, H. High Thermoelectric Performance of Type-III Clathrate Compounds of the Ba−Ge−Ga System. *Acta Mater.* **2006**, *54* (8), 2057−2062.

(18) Kim, J.-H.; Okamoto, N. L.; Kishida, K.; Tanaka, K.; Inui, H. Thermoelectric Properties and Crystal Structure of Type-III Clathrate Compounds in the Ba−Al−Ge System. *J. Appl. Phys.* **2007**, *102* (3), 034510.

(19) Kim, J.-H.; Okamoto, N. L.; Kishida, K.; Tanaka, K.; Inui, H. Crystal Structure and Thermoelectric Properties of Type-III Clathrate

Compounds in the Ba−In−Ge System. *J. Appl. Phys.* **2007**, *102* (9), 094506.

(20) Fukuoka, H.; Iwai, K.; Yamanaka, S.; Abe, H.; Yoza, K.; Häming, L. Preparation and Structure of a New Germanium Clathrate, $Ba_{24}Ge_{100}$. *J. Solid State Chem.* **2000**, *151* (1), 117−121.

(21) Kim, S.-J.; Hu, S.; Uher, C.; Hogan, T.; Huang, B.; Corbett, J. D.; Kanatzidis, M. G. Structure and Thermoelectric Properties of Ba_6Ge_{25-x}, $Ba_6Ge_{23}Sn_2$, and $Ba_6Ge_{22}In_3$: Zintl Phases with a Chiral Clathrate Structure. *J. Solid State Chem.* **2000**, *153* (2), 321−329.

(22) Carrillo-Cabrera, W.; Curda, J.; Von Schnering, H.; Paschen, S.; Grin, Y. Crystal Structure of Hexabarium Pentacosagermanide, Ba_6Ge_{25}. *Z. Kristallogr. - New Cryst. Struct.* **2000**, *215* (2), 207−208.

(23) Carrillo-Cabrera, W.; Curda, J.; Peters, K.; Paschen, S.; Grin, Y.; von Schnering, H. Crystal Structure of the Chiral Clathrate $Na_2Ba_4Ge_{25}$. *Z. Kristallogr. - New Cryst. Struct.* **2001**, *216* (1−4), 193−194.

(24) Okamoto, N. L.; Kim, J.-H.; Tanaka, K.; Inui, H. Splitting of Guest Aatom Aites and Lattice Thermal Conductivity of Type-I and Type-III Clathrate Compounds in the Ba−Ga−Ge System. *Acta Mater.* **2006**, *54* (20), 5519−5528.

(25) Carrillo-Cabrera, W.; Gil, R. C.; Paschen, S.; Grin, Y. Crystal Structure of Barium Europium Germanide, $Ba_{6-x}Eu_xGe_{25}$ (x= 0.6), a Chiral Clathrate. *Z. Kristallogr. - New Cryst. Struct.* **2003**, *218* (JG), 429−430.

(26) Deng, S.; Saiga, Y.; Kajisa, K.; Takabatake, T. High Thermoelectric Performance of Cu Substituted Type-VIII Clathrate $Ba_8Ga_{16-x}Cu_xSn_{30}$ Single Crystals. *J. Appl. Phys.* **2011**, *109* (10), 103704.

(27) Saiga, Y.; Suekuni, K.; Deng, S. K.; Yamamoto, T.; Kono, Y.; Ohya, N.; Takabatake, T. Optimization of Thermoelectric Properties of Type-VIII Clathrate $Ba_8Ga_{16}Sn_{30}$ by Carrier Tuning. *J. Alloys Compd.* **2010**, *507* (1), 1−5.

(28) Li, Y.; Gao, J.; Chen, N.; Liu, Y.; Luo, Z. P.; Zhang, R. H.; Ma, X. Q.; Cao, G. H. Electronic Structure and Physical Properties of $Ba_8Ga_{16}Sn_{30}$ Clathrates with Type-I and Type-VIII Structure. *Phys. B* **2008**, *403* (5−9), 1140−1141.

(29) Zheng, Y.; Zhang, Q.; Su, X.; Xie, H.; Shu, S.; Chen, T.; Tan, G.; Yan, Y.; Tang, X.; Uher, C.; Snyder, G. J. Mechanically Robust BiSbTe Alloys with Superior Thermoelectric Performance: A Case Study of Stable Hierarchical Nanostructured Thermoelectric Materials. *Adv. Energy Mater.* **2015**, *5* (5),10.1002/aenm.201401391

(30) Slack, G. A.; Hussain, M. A. The Maximum Possible Conversion Efficiency of Silicon-Germanium Thermoelectric Generators. *J. Appl. Phys.* **1991**, *70* (5), 2694.

(31) Liu, W.; Chi, H.; Sun, H.; Zhang, Q.; Yin, K.; Tang, X.; Zhang, Q.; Uher, C. Advanced Thermoelectrics Governed by a Single Parabolic Band: $Mg_2Si_{0.3}Sn_{0.7}$, a canonical example. *Phys. Chem. Chem. Phys.* **2014**, *16* (15), 6893−7.

(32) Tang, X.; Li, H.; Zhang, Q.; Niino, M.; Goto, T. Synthesis and Thermoelectric Properties of Double-atom-filled Skutterudite Compounds $Ca_mCe_nFe_xCo_{4-x}Sb_{12}$. *J. Appl. Phys.* **2006**, *100* (12), 123702.

(33) Shi, X.; Kong, H.; Li, C. P.; Uher, C.; Yang, J.; Salvador, J. R.; Wang, H.; Chen, L.; Zhang, W. Low Thermal Conductivity and High Thermoelectric Figure of Merit in n-type $Ba_xYb_yCo_4Sb_{12}$ Double-filled Skutterudites. *Appl. Phys. Lett.* **2008**, *92* (18), 182101.